Japanese Journal of Applied Physics **53**, 05HA09 (2014) **REGULAR PAPER**
http://dx.doi.org/10.7567/JJAP.53.05HA09

Numerical simulations of supersonic gas atomization of liquid metal droplets

Dudi Adi Firmansyah[1], Rashed Kaiser[1], Riyan Zahaf[1], Zach Coker[2], Tae-Youl Choi[2], and Donggeun Lee[1*]

[1]*School of Mechanical Engineering, Pusan National University, Busan 609-735, Republic of Korea*
[2]*Department of Mechanical and Energy Engineering, University of North Texas, Denton, TX 76203, U.S.A.*
E-mail: donglee@pusan.ac.kr

Received October 13, 2013; accepted February 28, 2014; published online April 28, 2014

Computational fluid dynamics simulations incorporating supersonic turbulent gas flow models and a droplet breakup model are performed to study supersonic gas atomization for producing micron-sized metal powder particles. Generally such atomization occurs in two stages: a primary breakup and a secondary breakup. Since the final droplet size is primarily determined by the secondary breakup, parent droplets of certain sizes (1 to 5 mm) typically resulting from the primary breakup are released at the corner of the nozzle and undergo the secondary breakup. A comparison of flow patterns with and without the introduction of a liquid melt clearly indicates that the mass loading effect is quite significant as a result of the gas–droplet interactions. The flow pattern change reasonably explains why the final droplets have a bimodal mass size distribution. The transient size changes of the droplets are well described by the behavior of the Weber number. The present results based on the 1 mm parent droplets best fit previous experimental results. Moreover, the effects of inlet gas pressure and temperature are investigated in an attempt to further reduce droplet size.

1. Introduction

Metal powders have been considered one of the main materials in powder metallurgy, with a large variety of applications including those to sintering processes[1)] and as thermal sprays,[2)] chemical catalysts,[3)] and rocket propellants.[4)] The methods of producing metal powders are divided into three main types: chemical, mechanical and physical methods.[5)] Among them, the physical method, i.e., gas atomization, remains a good choice owing to the versatility, quality, and purity of the obtained powders. This process also enables greater control of various powder properties and thus shows potential for mass production.[6)] The most widely employed atomization types in the industries are close-coupled atomization and free-fall atomization, which are distinguished based on the location of where the gas and melt jet meet.[7)] The gas exit is confined to the melt delivery tube in close-coupled atomization, whereas in free-fall atomization, there is a distance ranging from 10 to 30 cm between the exit of the melt feeding tube and the gas jet.[7)] Close-coupled atomization is more favorable for producing fine powders through better breakup of the liquid phase owing to the short distance between the gas jet and the metal melt.

Typical atomization can be generalized as a two-stage breakup process. In the first stage, i.e., primary atomization, the surface of the melt is disturbed by a sinusoidal oscillation induced by high-velocity gas jets, and is subsequently broken up into unstable bodies (ligaments) and large droplets.[8)] Imminently following the primary atomization breakup, a secondary breakup takes place to greatly reduce the droplet size before solidification starts.[9)] The detailed physics involved in gas atomization is not yet fully understood. Naturally, when gas enters a typical atomization nozzle [convergent or convergent–divergent (C–D) nozzles], it undergoes a large expansion. This expansion causes the flow to be supersonic, and such gas flow dynamics has been investigated by Unal[10)] and Mates and Settles.[11)] Both reported that C–D nozzles do not produce strong internal shocks, while convergent nozzles are highly underexpanded and their near-region is dominated by a strong internal shock. Both nozzles, however, produce similar supersonic jet lengths and particle size distributions at similar operating pressures. Interestingly, after introducing the melt, Mates and Settles captured the occurrence of the primary breakup close to the nozzle tip and the secondary breakup up to 10 nozzle diameters from the melt exit.[11)] Large unatomized droplets are observed downstream of the jet, while micron droplets exist in the outer region at the same distance. The ability of such coarse droplets to survive for such long distances in the high-velocity gas stream is an indicator of severe liquid mass loading effects. The strength of the gas core is weakened by the mass loading of the carried particles, which results in less effective atomization of the melt.[11)]

In the modeling aspect, atomization processes have been investigated intensively by treating the liquid phase as a discrete phase in a Lagrangian framework. Markus and Fritsching[12)] have developed a numerical simulation method by integrating primary and secondary breakup mechanisms with heat transfer in other solidification processes. Their results are compared with previous experimental results; however, their gas flow is still modeled as the flow of an incompressible gas which is not valid in the atomizer exit region, as the local Mach number could be higher than 1 for a fully expanded supersonic flow. Zeoli and Gu[9)] have neglected the primary breakup mechanism and only simulated the secondary breakup of liquid metal droplets using a combination of the Taylor analogy breakup (TAB) model and Kelvin–Helmholtz (KH) instability model, depending on the Weber number. They provided a consistent gas flow profile and proposed a multistage breakup of droplets based on particle diameter history throughout the domain. However, their particle trajectories were in poor agreement with the previous experimental results[11)] because they neglected the unsteady feature of droplet streaming. Sarkar et al.[13)] developed a numerical simulation method for the secondary breakup in a full-scale atomization chamber and proposed a direct droplet breakup process based on similar profiles of the Weber number and particle diameter along the symmetric axis. This model, however, does not apply for all gas–metal ratios (GMR). However, all these works still neglected two-way coupling, i.e., gas-to-droplet or droplet-to-gas coupling, so that liquid droplets cannot affect the gas phase. Two-way coupling not only relates to the aforementioned mass loading effect that can reduce the jet core strength, but also

contributes to unsteady features of atomization.[11] In the present work, therefore, we employ the two-way droplet-to-gas coupling to realize the mass-loading effect in the secondary atomization of droplets, and to simulate more realistic atomization experiments and therefore elucidate the breakup process.

2. Model description

Upon contact with a high-speed gas jet, the melt breaks up into large droplets with a diameter of up to 500 μm (primary breakup). These droplets undergo further disintegration in flight to produce finer powders (secondary breakup).[14] Experimental studies of single particles have shown that a liquid droplet subjected to a gas flow becomes increasingly flattened and then exhibits one of the following two breakup behaviors: if the gas velocity is equal to or slightly above the critical velocity required to cause the shattering of the drop, the drop is blown out into the form of a hollow bag attached to a roughly circular rim. This bag subsequently bursts and produces a shower of fine drops, and the rim breaks up further into larger drops which comprise about three-quarters of the liquid in the original drop.[14] This type of breakup is known as the bag breakup. Note that the coarse and fine particles produced in this process are formed from two different parts of the original drop, and thus the particles are distributed in a wide size range.

If the gas velocity greatly exceeds the critical value, the drop deforms in a manner opposite to that of bag breakup and forms a convex surface relative to the gas flow. The edges of the saucer shape are drawn out into a thin sheet and then torn into ligaments which are later broken into smaller droplets. This mechanism is known as the stripping breakup. In addition to these two kinds of main breakup mechanisms, at a low relative velocity, the droplets vibrate and sometimes break into two smaller droplets (vibration mechanism), but this is a relatively slow process and thus is unlikely to be of importance in gas atomization.[14]

The main parameter related to breakup physics is the Weber number[9] defined as

$$We = \frac{\rho_g U_{rel}^2 r_p}{\sigma}, \tag{1}$$

where ρ_g is the gas density, U_{rel} is the relative velocity of gas with respect to slowly moving droplet, r_p is the parent droplet radius, and σ is the surface tension of the melt droplet.[9] More recently, two different numerical models have been distinctively used for breakup simulations, depending on the Weber number: the TAB model and KH instability model. It is known that the TAB model works better in the bag breakup (usually for $We < 80$) and the KH model provides strong agreement with experimental data in the stripping breakup ($We > 80$).[9] For instance, Liu et al.[15] showed from their simulations that the KH model exhibits better agreement with the experimental results in a high-speed gas jet, and that the TAB model underestimated final particle size. More recently, Zeoli and Gu[9] have used both models in their simulations, but there was no substantial difference in the mean particle diameter: ~39.9 μm from the combined use of both models vs 38.8 μm from the use of only the KH model. Thus, the KH model is only employed for simplicity in the present work. This model takes into account the fastest growing disturbance on the surface of droplets, which most probably will result in breakup. The wavelength of this disturbance Λ is[15]

$$\frac{\Lambda}{r_p} = \frac{9.02(1 + 0.45Z^{0.5}(1 + 0.4\Gamma^{0.7})}{(1 + 1.45We)^{0.6}}, \tag{2}$$

where Z is the Ohnesorge number and Γ is the Taylor number. The maximum growth rate of the surface wave Ω is

$$\Omega\left(\frac{\rho_l r_p^3}{\sigma}\right)^{0.5} = \frac{(0.34 + 0.38We^{1.5})}{(1 + Z)(1 + 1.4\Gamma^{0.6})}. \tag{3}$$

The radius of droplets, r, resulting from the atomization is proportional to the wavelength of the fastest-growing unstable surface wave:

$$r = B_0\Lambda, \tag{4}$$

where B_0 is a model constant equal to 0.61 based on the results of Reitz analysis. The characteristic breakup time t_b is given by[15]

$$t_b = \frac{3.726B_1 r_p}{\Omega\Lambda}, \tag{5}$$

where the B_1 is an adjustable model constant with a different value in each breakup regime. In Reitz analysis it was assumed that $B_1 = 10$. To model the stretching and thinning mechanism of "child" droplets pinching from the "parent" droplet, the rate of decrease in the radius of the parent droplets is denoted by

$$\frac{dr_p}{dt} = \frac{r_p - r}{t_b}. \tag{6}$$

The radius of parent droplets is assumed to be invariant unless the mass removal [according to Eq. (6)] reaches 3% of its initial mass.[9]

3. Model implementation

The secondary breakup model described above is implemented for a close-coupled gas atomization environment in the commercial code Ansys Fluent 13. The computational domain is based on the conventional C–D slit nozzle (CDSN)[4,16] shown in Fig. 1. The grid has a cell number of 20429 and an additional grid sensitivity test confirms that further increasing the grid density has not produced any change in flow pattern. The structured grid can capture all of the flow characteristics and provide consistent flow predictions to the compressible flow theories and previous works.[9] The computation is performed as an unsteady simulation. To ensure accuracy of the results and avoid any problems with solution convergence, very small time steps of 1×10^{-5} and 5×10^{-7} s are employed for the gas-phase simulation and gas–droplet (discrete phase model) simulation, respectively. The gas-phase equations, represented by the Reynolds-stress turbulence model,[9,17] are fully coupled with a discrete phase model to account for the effect of gas-to-droplet and droplet-to-gas interactions during atomization. The liquid spray is treated as a number of parcels that contain a given number of droplets with the same mass, momentum and physical properties as described in Table I. The nozzle normally operates at a reservoir pressure of 11 atm. This pressure is used as a basic inlet boundary condition for the gas flow simulations unless otherwise noted. The pressure at the outlet boundary is set to 1 atm. The gas-phase fluid is nitrogen,

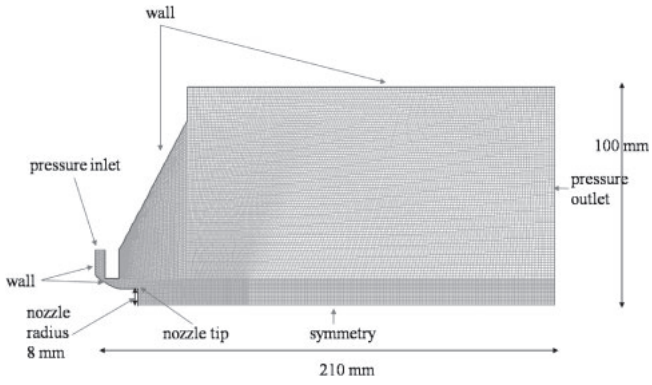

Fig. 1. Geometry of computational domain and boundary conditions.

Table I. Material properties of molten metal.

Property	Value	Reference
H. Latent heat ($J\,kg^{-1}$)	250 000	9
C liquid ($J\,kg^{-1}\,K^{-1}$)	825	9
Density ($kg\,m^{-3}$)	7700	9
Viscosity ($kg\,m^{-1}\,s^{-1}$)	0.0056	9
Thermal conductivity ($W\,m^{-1}\,K^{-1}$)	16.3	9
Surface tension ($N\,m^{-1}$)	1.2	9
Boiling point (K)	3003	22
Vaporization point (K)	2273	22
Saturaion vapor pressure (atm)	3.9872×10^{-5}	23

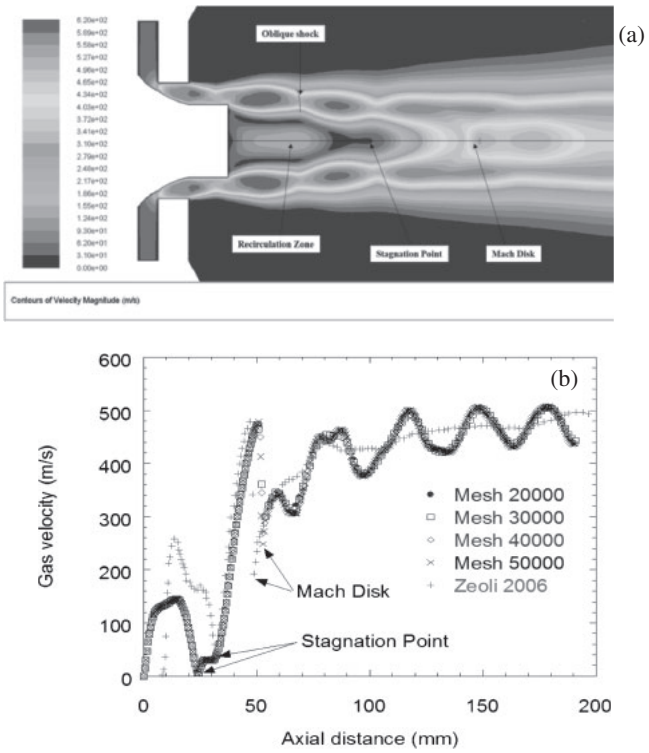

Fig. 2. Characteristics of gas flow without introduction of the melt. (a) contour plot of gas velocity magnitude and (b) velocity profiles of gas flow along the symmetry axis obtained from four different grid systems in comparison with those in previous simulation works.

modeled as compressible gas following the ideal gas law, and the other properties are taken from the database of the commercial code used. The inlet gas temperature is set to 300 K as a basic condition and then varied to 500 and 700 K. The boundary conditions are also illustrated in Fig. 1. The wall denotes an adiabatic wall boundary. Once the gas flow field develops to reach the steady state in the chamber, liquid metal droplets with a temperature of 1900 K are released at the corner (tip) of the melt feeding tube at a mass flow rate of 0.27619 kg/s corresponding to a GMR of 1.1. The mean particle diameter is measured at the exit repeatedly at specific time intervals, for example, every 1 ms, until the droplet size becomes time-independent. The obtained final size distributions of the droplets are compared with the previous experimental results. The experimental parameters such as the temperature and pressure of the inlet gas are also investigated in an attempt to further reduce the droplet size.

4. Results and discussion

4.1 Gas flow dynamics

The gas flow inside the atomization chamber is firstly studied without introducing a liquid metal. The velocity flow field is shown in Fig. 2(a) which demonstrates the formation of a series of shocks from the supersonic jet. This flow field is consistent with the theoretical descriptions of compressible flow and high-speed jets in the literature.[9,18,19] As soon as the gas jet enters the chamber, it rapidly expands owing to the large pressure difference between the exit of the nozzle and the chamber. This gives rise to a high-speed turbulent compressible flow inside the chamber, which reaches a maximum velocity of 620 m/s or a maximum Mach number of 1.8. As a result, the gas expands through a series of waves and oblique shocks immediately after entering the chamber.[9,13] It is also observed that, as the high-pressure gas enters the nozzle, the sharp angle of the gas flow with respect to the nozzle causes the detachment of the flow from the wall, and a recirculation flow is generated around the corner of the melt tube end. This recirculation zone is characterized by a separation of turbulent layers in the upstream and downstream flows, which is consistent with the experimental observation.[11] At the end of this recirculation zone, there is a stagnation front, where the gas velocity falls to approximately zero as quantitatively shown by the velocity diagram in Fig. 2(b). Furthermore, Fig. 2(b) also clearly shows the formation of a Mach disk, the velocity oscillation behavior, and the presence of shock in the gas flow field, with reasonable agreement with Zeoli and Gu's[9] velocity profile.

Figure 3 shows the gas flow fields before and after introducing the melt to the entire atomization domain. Before introducing the melt, the gas flow field exhibits a classic repeating shock "diamond" pattern, typical of an imperfectly expanding gas jet produced by round nozzles.[11] When liquid metal droplets are introduced, the gas flow field that normally crosses completely through the middle of the jet to form large shock diamonds pattern changes to form much smaller diamonds.[11] This flow pattern change is one indication of severe mass loading effects.[11] It was reported that the mass loading effect in a two-phase flow of similar geometry is significant even for mass loading ratios as small as 0.1%.[20] In the present study, the mass loading ratio (defined as the ratio of the dispersed-phase mass flow rate to the continuous-

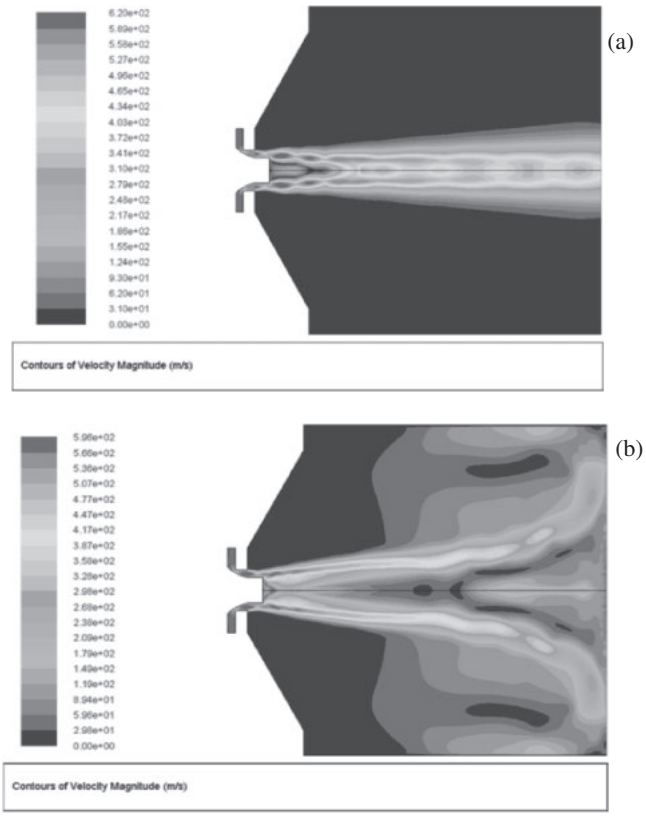

Fig. 3. Gas flow patterns in the entire atomization chamber; (a) without and (b) with introduction of the melt.

phase mass flow rate) is on the order of 95% (corresponding to GMR = 1.1). As indicated in Fig. 3(b), this loading effect substantially reduces the overall gas velocity and causes a significant radial velocity gradient in the jet core. This effect has never been reported in previous atomization simulation studies[7,9,13] not considering gas–particle interaction and will be discussed further in the context of droplet breakup dynamics in the following section.

4.2 Droplet breakup dynamics

As described in Sect. 2, the breakup process basically entails two steps: primary breakup and secondary breakup.[9,14] Since the final droplet size is mainly determined by the secondary breakup,[11] the primary breakup is excluded in this study as in previous simulation studies.[9,14] For instance, Mates and Settles[11] reported that finer droplets with a higher population were produced at a higher operating pressure, attributed to the elongation of the supersonic region of gas jet and the resultant extension of the secondary breakup. Experimental studies[19,21] have shown that the droplet size after the primary breakup is about 10–100% of melt nozzle diameter. Therefore, regarding the melt tube of 8 mm diameter, droplets of 1, 3, and 5 mm sizes are considered. These droplets are continuously released at the corner of the melt tube to undergo the secondary breakup. The behaviors of melt droplets are simulated by the Lagrangian discrete phase model, which can track the motion and size change of droplets, as shown in Fig. 4(a). It is found that the droplet trajectories during atomization appear to be similar to the classic comet-like appearance of droplets photographed in a previous work.[11]

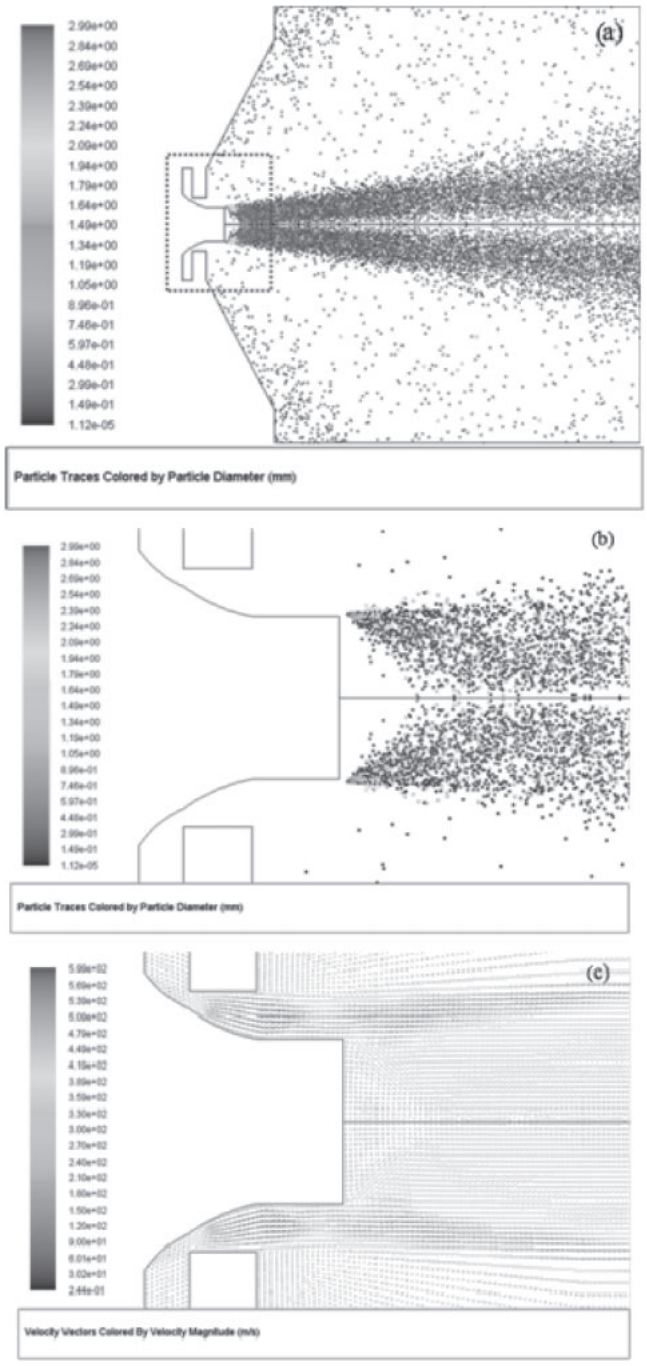

Fig. 4. (a) A snapshot of atomization occurring in the chamber, (b) magnified image of the snapshot where colored dots represent droplets of different sizes, and (c) vector plot of gas velocity in the magnified region.

The colors in Fig. 4(a) represent droplets of different sizes. Figure 4(a) shows that parent droplets in red undergo a fast breakup process, turning red dots (3 mm) into yellow (~2 mm), green (~1.5 mm), and blue (≤150 μm) dots within a short distance of 20 mm from the tube end. Since this breakup occurs predominantly near the nozzle, this region denoted by a dotted box in Fig. 4(a) is enlarged and shown in Fig. 4(b). Prior to describing breakup in detail, gas flow behavior in the enlarged region is first investigated as shown in Fig. 4(c). Figure 4(c) shows that the gas flow undergoes a large velocity gradient perpendicular to the streamwise direction, near the corner of the melt tube. For instance, local gas speed decreases from 599 m/s (red arrow) to 300 m/s

over a short radial distance of 1.3 mm, starting from the corner. From Fig. 4(c), also note that there are two distinct characteristics of the gas flow: 1) the main stream of an annular supersonic gas jet with a gradual outward expansion denoted by reddish streaks, and 2) an inward radial flow detached from the main stream followed by a subsequent outward expansion, as denoted by yellow and yellowish-green (low-speed) colors near the tube end.

Keeping the flow characteristics in mind, we investigate how a single parent droplet behaves in the gas flow by tracking it. When a parent droplet is released near the corner (where the gas velocity is highest), a series of blue (50–70 μm in diameter) child droplets are constantly produced from the parent droplet, causing a gradual size reduction of the parent droplet. These child droplets, immediately after departing from their parent, tend to spread out toward the annular gas jet boundary and drift downstream much faster than the parent droplet. They are already so small that their Weber number decreases below 10, where further atomization (fragmentation) is not allowed. On the other hand, the parent droplet moves along the radial inward flow up to a point ~8 mm downstream from the tube end ($x \leq 8$ mm) and then moves outward up to a point ~8 mm away from the symmetric axis owing to the oscillatory gas flow pattern. Since the relative velocity [U_{rel} in Eq. (1)], that the droplet takes, decreases significantly in the first region of $x \leq 8$ mm, atomization from the parent droplet ceases until the droplet enters the second region. In the second region, the relative velocity recovers to some degree, restarting atomization from the parent droplet.

Upon continuous release of 3 mm parent droplets, fast-moving child droplets catch up with and pass other parent droplets that have been released earlier. This is why coarse (parent) droplets coexist with micrometer (child) droplets at a certain axial distance (x) from the tube end, as shown in Figs. 4(a) and 4(b). In order to quantitatively explore the size reduction of droplets during their atomization, we sample droplets existing at a certain axial distance and extract their sizes.

Figure 5(a) shows droplet diameters sampled at different axial positions (x) as a function of the radial distance from the nozzle axis. As shown by red dots, droplets at $x = 1$ mm have diameters of 2.7–3 mm and are distributed in a very narrow region at a radial distance of approximately 8 mm. It is clear that those parent droplets become smaller and gradually disperse moving downstream. At $x = 3$ mm, child droplets as small as ~0.1 mm appear together with parent droplets of ~2.2 mm, indicative of the vigorous breakup in the radial region of 7–9 mm. This is exactly consistent with the distribution of *We* in Fig. 5(b). In addition, the *We* of the droplets at $x = 3$ mm very rapidly decreases with the radial position change from 9 to 7 mm, which is attributed to very high gradient of the radial velocity of gas. Moving further downstream up to 20 mm (x), the diameter of parent droplets decreases to 1.1 mm, while slightly larger new child droplets are born. The generation of large child droplets is attributed to the less effective breakup resulting from the fact that parent droplets with smaller diameters of $5 \leq x \leq 20$ mm are broken up by a lower-velocity gas flow, achieved by lowering the *We*. Also, as shown in Fig. 5(b), the *We* markedly decreases along the axis, making the breakup less vigorous. Droplets

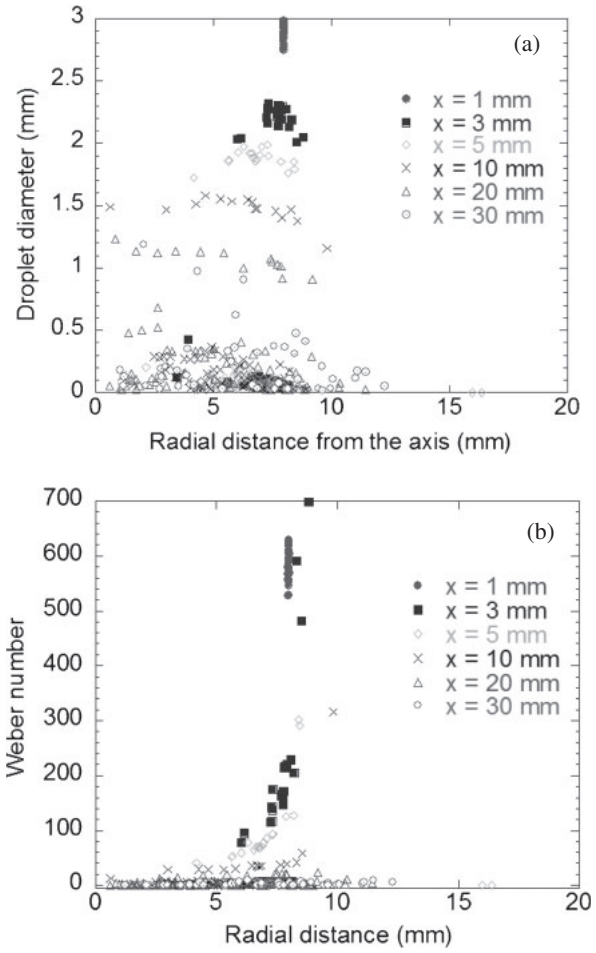

Fig. 5. (a) Radial distributions and diameters of droplets and (b) the corresponding *We* values of droplets at different axial distances from the melt tube end.

existing in the radial position of 3–10 mm at $x = 20$ mm have $We > 10$ so that they are allowed for further breakup. On the other hand, almost all droplets at $x = 30$ mm have a very small *We*, suggesting no more breakup downstream of this axial position, as confirmed in Fig. 5(a).

Figure 6 shows the transient behaviors of the average diameter and size distribution of droplets monitored at the exit boundary of the calculation domain upon continuous release of 3 mm coarse droplets. Figure 6(a) shows that the size of the droplets gradually increases from ~26 to ~70 μm for the first 50 ms, and then is almost invariant. The size increase at the beginning is explained as follows. From the single-droplet analysis, child droplets arrive at the exit boundary within 3.6 ms. Therefore, only some of the child droplets can arrive at their destination and be detected within a short time of 2 ms. This is why a narrow and unimodal size distribution of droplets is observed at 2 ms in Fig. 6(b). With time, the unimodal distribution clearly turns into a bimodal distribution having two mode diameters of 30 and 56 μm. In Fig. 6(b), the population of droplets larger than 56 μm obviously increases with time up to 30 ms, resulting in a rapid increase in the mean diameter of droplets in Fig. 6(a). Those 56 μm droplets begin to arrive at the exit later than the smaller ones, making the size distribution wider and bimodal. Such a bimodal distribution might be related to the two different routes of gas flow explained in Fig. 4(c). Coarse

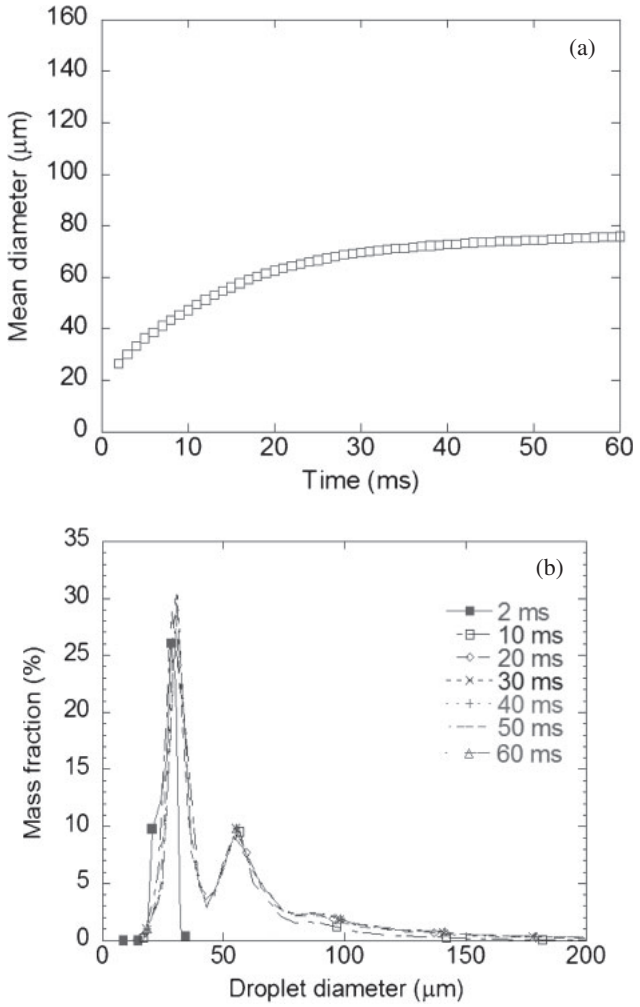

Fig. 6. (a) Transient behavior of mean diameter of droplets with increasing time and (b) mass size distributions of droplets obtained at different times.

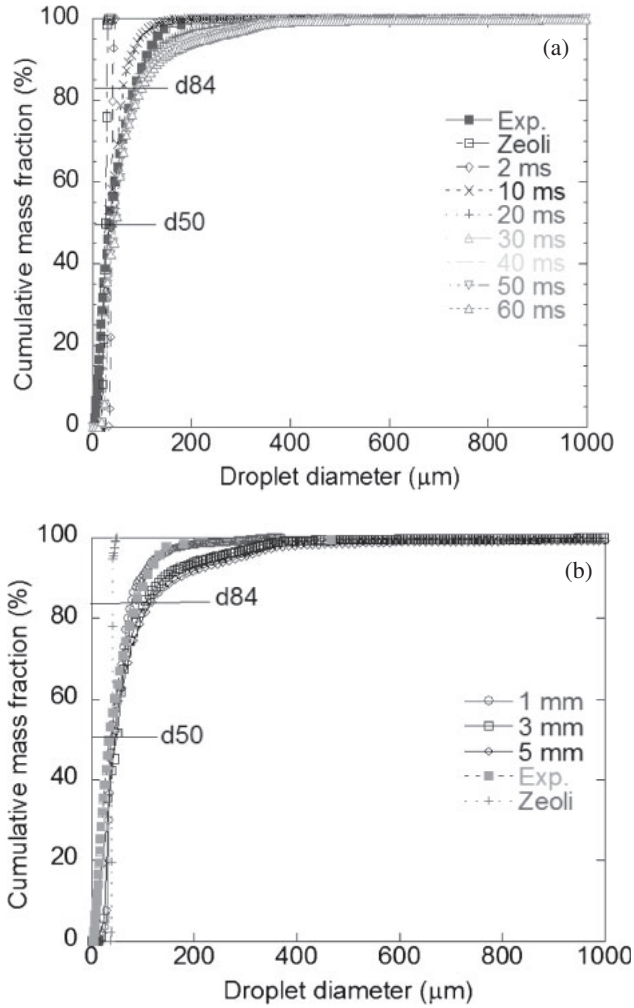

Fig. 7. Cumulative mass size distributions of droplets generated upon continuous release of (a) 3 mm and (b) three coarse droplets of different sizes, measured at the exit boundary at different times.

droplets taking the first route (main stream of annular supersonic gas jet) undergo a very fast breakup to produce the smallest child droplets, which might be the primary-mode droplets (30 μm). On the other hand, coarse droplets taking the second route (denoting the low-*We* track) tend to produce relatively large child droplets slowly for a longer time period.

On the basis of Fig. 6(b), the mass-based cumulative size distributions of droplets are calculated at different times and compared with Zeoli and Gu's result[9] and Anderson and Terpstra's experimental result[16] in Fig. 7(a). Note that our cumulative size distribution departs from Zeoli and Gu's and is close to the experimental curve with time (10–20 ms). Beyond 50 ms, there is no substantial change in the distribution, indicating that the system has reached a steady-state condition. Also note that a type of shoulder (or bending) is observed in the distribution curve, indicative of a mode change. In the figure, two diameters d_{50} and d_{84} are shown since the ratio of d_{84}/d_{50} is often used as a measure of the width of particle size distribution. d_{50} and d_{84} are defined as droplet diameters to which the cumulative mass fraction reaches 50 and 84%, respectively. Figure 7(b) shows the size effect of the initial parent droplets on the final size of micron droplets. As smaller parent droplets are used, the cumulative size distribution is closer to the experimental curve and best fitted in the case of 1 mm. Parent droplets larger than 3 mm in diameter do not show a remarkable change in their distribution. As summarized in Table II, the d_{50} in the case of 1 mm shows the best agreement with the experimental value, while the experimental d_{84} lies between the values in the two cases of 1 and 3 mm. It is therefore speculated that 1–2 mm coarse droplets are likely produced by the primary breakup in an actual situation, prior to the subsequent secondary breakup.

Table II. Comparison of present calculation results with previous simulation and experimental results.

Parent droplet diameter (mm)	d_{50} (μm)	d_{84} (μm)	d_{84}/d_{50}
1	37.3	79.6	2.1
3	42.3	102	2.4
5	44.8	117	2.6
Experiment[15]	37.3	84.6	2.3
Simulation[9]	39.8	42.8	1.1

In an attempt to further reduce the final droplet size, the effects of inlet pressure and temperature are explored for a parent droplet of 1 mm. In Fig. 8(a), when the inlet pressure

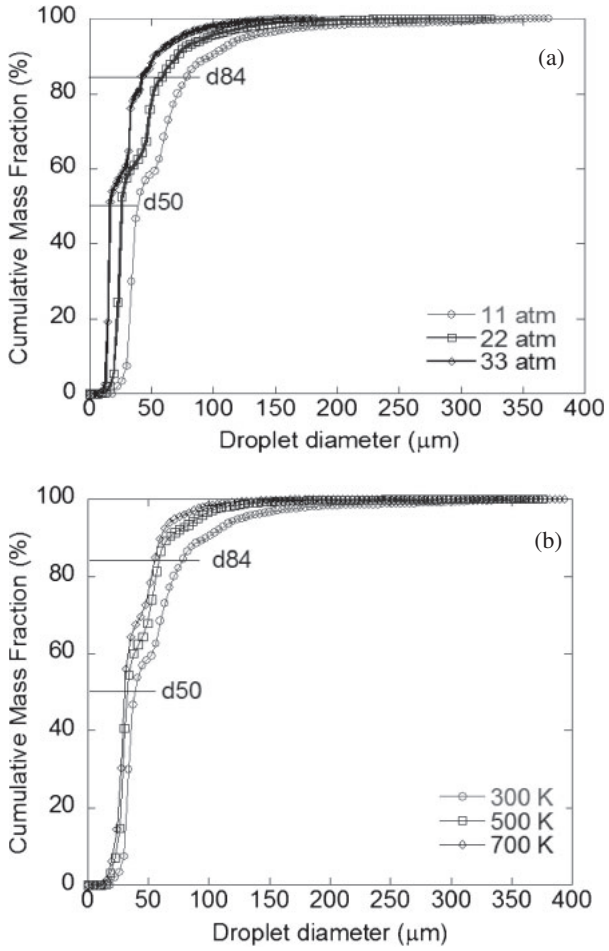

Fig. 8. Effects of (a) inlet gas pressure and (b) gas temperature on the final cumulative mass size distributions of droplets.

is increased from 11 to 33 atm, the cumulative mass distribution is shifted to smaller sizes almost proportionally: a significant decrease in d_{50} from 39.8 to 14.9 μm. Such a large size reduction is attributed to a higher gas velocity at a higher inlet pressure as follows. Applying Anderson and Terpstra's results[16] to the current simulation conditions, we estimate the inlet mass flow rate of gas. When the inlet pressure increases from 11 to 33 atm, the mass flow rate increases significantly from 0.29 to 1.11 kg/s corresponding to a GMR of 4. Since a higher mass flow rate of the gas jet produces a strengthened and elongated supersonic zone, a condition of high inlet pressure is preferable for producing smaller droplets.[19] Figure 8(b) shows the effect of gas temperature on the mass median diameter d_{50}: a hotter gas atomization could produce smaller metal droplets. This is similarly attributed to the increase in inlet gas velocity, resulting from a density decrease at a fixed mass flow rate, when increasing temperature. This effect is expected to be more pronounced in an actual situation in which the surface tension of droplets can be reduced more at higher gas temperatures.

5. Conclusions

In this study, hot gas atomization was numerically simulated to better understand details of the phenomenon. Unsteady, turbulent, supersonic gas flow and droplet behavior including fragmentation were calculated along with the a two-way coupling between gas and droplets unlike in previous simulation works. We demonstrated for the first time that the streaming of fine droplets in a gas flow causes a significant change in the gas flow pattern, especially near the nozzle. The flow pattern change was confirmed to be the key to explain the bimodal mass size distribution of product droplets and to best fit the previous experimental result as well. The size changes of droplets are well described by the behavior of *We*. Moreover, inlet gas pressure and temperature were chosen as practical systematic parameters for further reduction in droplet size. The final mass median diameters of droplets could be reduced almost linearly with increasing pressure. Temperature was also considered to be a good parameter.

Acknowledgements

This work was supported by the National Research Foundation of Korea (NRF), by grants funded by Ministry of Science, ICT and Future Planning (MSIP) (No. 2010-0019543), by the R&D Convergence Program of the MSIP and ISTK (Korea Research Council for Industrial Science and Technology) of Republic of Korea (Grant B551179-12-02-00), and finally by the Human Resources Development program (No. 20124010203230) of the Korea Institute of Energy Technology Evaluation and Planning (KETEP) grant funded by the MOTIE.

1) H.-X. Chen, Y.-T. Tsai, and K.-H. Lin, Proc. World Congr. Engineering III, 2013, p. 1825.
2) N. Zeoli, H. Tabbara, and S. Gu, Chem. Eng. Sci. **66**, 6498 (2011).
3) D. Cheng, H. Ma, D. Cao, and F. Ding, Mater. Sci. Forum **534–536**, 41 (2007).
4) B. Cjazka, K. Pruchniak, and L. Wachowski, Mater. Wysokoenergetyczne **4**, 36 (2013) [in Polish].
5) O. D. Neikov, S. Naboychenko, I. B. Mourachov, V. G. Gopienko, I. V. Frisberg, and D. V. Lotsko, *Handbook of Non-Ferrous Metal Powders: Technologies and Applications* (Elsevier, Amsterdam, 2009) 1st ed.
6) H. A. Kuhn and A. Lawley, *Powder Metallurgy Processing: New Techniques and Analyses* (Academic Press, New York, 1978).
7) N. Zeoli and S. Gu, Comput. Mater. Sci. **42**, 245 (2008).
8) G. Antipas, Metals **2**, 202 (2012).
9) N. Zeoli and S. Gu, Comput. Mater. Sci. **38**, 282 (2006).
10) A. Ünal, Metall. Trans. B **20**, 613 (1989).
11) S. P. Mates and G. S. Settles, At. Sprays **15**, 19 (2005).
12) S. Markus and U. Fritsching, Int. J. Powder Metall. **42**, 23 (2006).
13) S. Sarkar, S. Pimpalnerkar, B. Rogberg, P. Sivaprasad, and S. Bakshi, 24th Eurpoean Conf. Liquid Atomization and Spray Systems, 2011, p. 1.
14) A. Ünal, Metall. Trans. B **20**, 61 (1989).
15) A. Liu, D. Mather, and R. Reitz, SAE Tech. Pap., 930072 (1993).
16) I. E. Anderson and R. Terpstra, Mater. Sci. Eng. A **326**, 101 (2002).
17) B. E. Launder, G. J. Reece, and W. Rodi, J. Fluid Mech. **68**, 537 (1975).
18) J. Ting and I. E. Anderson, Mater. Sci. Eng. A **379**, 264 (2004).
19) J. Mi, R. S. Figliola, and I. E. Anderson, Mater. Sci. Eng. A **208**, 20 (1996).
20) J. Borée, T. Ishima, and I. Flour, J. Fluid Mech. **443**, 129 (2001).
21) S. Markus, U. Fritsching, and K. Bauckhage, Mater. Sci. Eng. A **326**, 122 (2002).
22) S. Lagutkin, L. Achelis, S. Sheikhaliev, V. Uhlenwinkel, and V. Srivastava, Mater. Sci. Eng. A **383**, 1 (2004).
23) M. Bober and J. Singer, High Temperature Vapor Pressures of Stainless Steel Type 1.4970 and some other Pure Metals from Laser Evaoration, 1984, KfK 3772.